J|A|C|S
ARTICLES
Published on Web 04/06/2002

Bcc and Fcc Transition Metals and Alloys: A Central Role for the Jahn−Teller Effect in Explaining Their Ideal and Distorted Structures

Stephen Lee* and Roald Hoffmann*

Contribution from the Department of Chemistry and Chemical Biology, Baker Laboratory, Cornell University, Ithaca, New York 14853-1301

Received June 14, 2001. Revised Manuscript Received September 4, 2001

Abstract: Transition metal elements, alloys, and intermetallic compounds often adopt the body centered cubic (bcc) and face centered cubic (fcc) structures. By comparing quantitative density functional with qualitative tight-binding calculations, we analyze the electronic factors which make the bcc and fcc structures energetically favorable. To do so, we develop a tight-binding function, ΔE_{star}, a function that measures the energetic effects of transferring electrons within wave vector stars. This function allows one to connect distortions in solids to the Jahn−Teller effect in molecules and to provide an orbital perspective on structure determining deformations in alloys. We illustrate its use by considering first a two-dimensional square net. We then turn to three-dimensional fcc and bcc structures, and distortions of these. Using ΔE_{star}, we rationalize the differences in energy of these structures. We are able to deduce which orbitals are responsible for instabilities in seven to nine valence electron per atom (e^-/a) bcc systems and five and six e^-/a fcc structures. Finally we demonstrate that these results account for the bcc and fcc type structures found in both the elements and binary intermetallic compounds of group 4 through 9 transition metal atoms. The outline of a theory of metal structure deformations based on loss of point group operation rather than translational symmetry is presented.

Introduction

As chemists, compare our understanding of discrete molecules and alloy structures. In molecular chemistry one has both quantum mechanical methods which allow the accurate determination of the electronic energy and simple orbital models useful in the rationalization of these ab initio results.[1−4] Chemists thus have a varied and vivid picture of why ammonia is pyramidal, $Cr(CO)_6$ octahedral, and $C_2B_{10}H_{12}$ an icosahedron. For some extended structures (e.g. covalent solids and Zintl phases, in which ionic and covalent bonding coexist) our understanding approaches that we have for molecules.

The situation is quite different for alloys and intermetallics. Although we have powerful tools such as density functional theory (DFT)[5−8] which permit the routine geometrical optimization of many structures, and there is a rich literature of model concepts for such systems,[9−23] the central theoretical framework of the structure determining factors in alloys and intermetallics remains elusive to the chemistry community as a whole. For the practicing solid state chemist, our understanding of even the simplest of alloy structures, the face centered cubic (fcc), body centered cubic (bcc), and hexagonal closest packings (hcp), is not nearly as sharp as the molecular chemist's understanding of the quite complex molecules.[24]

* To whom correspondence should be addressed. E-mail: S.L., sl137@cornell.edu; R.H., rh34@cornell.edu.

(1) Woodward, R. B.; Hoffmann, R. *The Conservation of Orbital Symmetry*; VCH: Weinheim, Germany, 1970.
(2) Fleming, I. *Frontier Orbitals and Organic Chemical Reactions*; J. Wiley: London, 1976.
(3) Albright, T. A.; Burdett, J. K.; Whangbo, M.-H. *Orbital Interactions in Chemistry*; J. Wiley: New York, 1985.
(4) Hehre, W. J.; Radom, L.; v. R. Schleyer, P.; Pople, J. A. *Ab Initio Molecular Orbital Theory*; J. Wiley: New York, 1986.
(5) Hohenberg, P.; Kohn, W. *Phys. Rev.* **1964**, *136*, B 864.
(6) Kohn, W.; Sham, L. J. *Phys. Rev.* **1965**, *140*, A 1133.
(7) Jones, R. O.; Gunnarsson, O. *Rev. Mod. Phys* **1989**, *61*, 689.
(8) Payne, M. C.; Teter, M. P.; Allan, D. C.; Arias, T. A.; Joannopoulos, J. D. *Rev. Modern Phys.* **1992**, *64*, 1045.
(9) Friedel, J. Electronic Structure of the d-band. Its Role in the Crystalline and Magnetic Structures. In *Physis of Metals*; Ziman, J. M., Ed.; Cambridge Press: London, 1969; p 340.
(10) Heine, V.; Weaire, D. *Solid State Phys.* **1970**, *24*, 249.
(11) Ducastelle, F.; Cyrot-Lackmann, F. *J. Phys. Chem. Solids* **1971**, *32*, 285.
(12) Hoffmann, R. *Solids and Surfaces*: *A Chemist's View of Bonding in Extended Structures*; VCH: New York, 1988.
(13) Burdett, J. K. *Chemical Bonding in Solids*; Oxford: New York, 1995.
(14) Pettifor, D. *Bonding and Structure of Molecules and Solids*; Oxford University Press Inc.: New York, 1995.
(15) Iung, C.; Canadell, E. *Description Orbitalaire de la Structure Électronique des Solides*; Ediscience: Paris, 1997.
(16) Chu, F.; Mitchell, T. E.; Chen, S. P.; Sob, M.; Siegl, R.; Pope, D. P. *J. Phase Equilib.* **1997**, *18*, 536.
(17) Zhang, C.; Hu, P.; Alavi, A. *J. Am. Chem. Soc.* **1999**, *121*, 7931.
(18) Vitos, L.; Raban, A. V.; Skriver, H. L.; Kollar, J. *Surf. Sci.* **1998**, *411*, 186.
(19) Soderlind, P.; Yang, L. H.; Moriarty, J. A.; Wills, J. M. *Phys. Rev. B*: *Condens. Matter. Phys.* **2000**, *61*, 2579.
(20) Häussermann, U.; Simak, S. I.; Ahuja, R.; Johansson, B. *Angew. Chem., Int. Ed.* **2000**, *39*, 1246.
(21) Landrum, G. A.; Dronskowski, R. *Angew. Chem., Int. Ed.* **2000**, *39*, 1560.
(22) Matar, S. F.; Mavromaras, A. *J. Solid State Chem.* **2000**, *149*, 449.
(23) Burdett, J. K.; Lee, S. *J. Am. Chem. Soc.* **1985**, *107*, 3063.
(24) There are notable theories which account for much of the structural chemistry of metals and alloys. See refs 9−11, 13, 14, and 23. But often these theoretical analyses are based on concepts not widely used in molecular chemistry (e.g., concepts such as the nodes in the pseudopotential function or the use of the various moments of the electronic density of states).

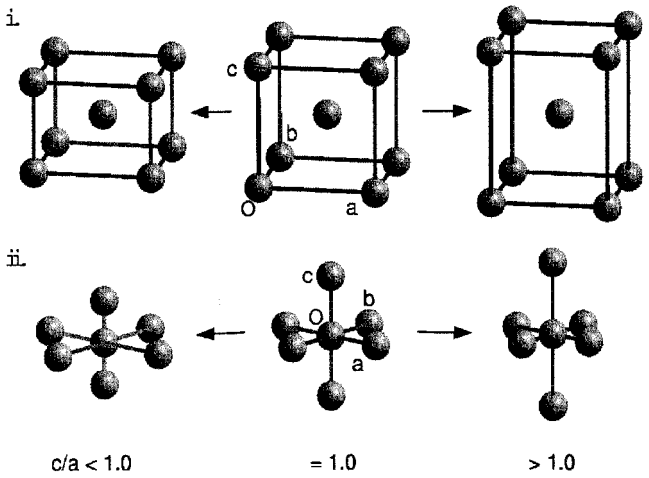

Figure 1. D_{4h} to O_h to D_{4h} distortion for (i) the body centered tetragonal (bct) structure and (ii) an octahedron.

The goal of this paper is to build toward an understanding of alloy and intermetallic structure using concepts already familiar to the chemistry community. Our focus is initially on the bcc and fcc structures. We begin with DFT calculations (details provided in the section on calculational methods), not as a tool to rationalize or predict structures, but essentially as a numerical laboratory.

Consider a metal, say tungsten, in a body centered tetragonal or bct cell, a structure in which there are two atoms in the conventional unit cell, one at the cell corner and the other at the body center (Figure 1i). On the left side of Figure 2 we show the DFT energy of this cell as a contour surface.[25] As variables, the obvious unitless parameter, c/a, the axis ratio, is employed, as well as $V/V_{\min}$. The latter parameter is the ratio of the given unit cell volume to the cell volume of the minimum energy structure. The energy minima of this surface are at $c/a \cong 1.0$ and 1.7, with a saddlepoint at $c/a = \sqrt{2}$ between them.

Contrast this tungsten surface with that of its neighbor in the periodic table, rhenium (Figure 2, middle left). Re has one more valence electron per atom (e^-/a), and its energy surface is markedly different from that of W. For example in Re, $c/a = \sqrt{2}$ is not a saddlepoint but an energy minimum. This change is even more pronounced if we keep the number of valence electrons per atom the same as Re but introduce ionicity—indeed one of the aims of our work is a theory of the geometric stability of alloy structures. Consider TaIr, a compound based on the elements two steps to the left and right of Re in the periodic table. As Ir is significantly more electronegative than Ta, the Ta−Ir bond is partially ionic. Here we find the surface shown at the bottom of Figure 2: the $c/a = 1.0$ structure is a saddlepoint, the global energy minimum is at $c/a = \sqrt{2}$, and a second local minimum is found near $c/a = 0.85$.[26]

Such multi-valley electronic surfaces are well-known in alloys and metals.[27−31] Many of the transtion metal elements have energy surfaces with a global minimum for one value of c/a and local minima at yet other values. Nor are these local minima calculational artifacts. Although in certain cases these local minima are not stable to nontetragonal distortion modes, for some transition metals it has even proven possible in epitaxially grown thin films to isolate metastable phases which directly correspond to the predicted local minima structures.[32−37]

In both the previously reported electronic surfaces and in the electronic surfaces shown in Figure 2, both c/a of 1.0 and $\sqrt{2}$ are energetically important in this body centered tetragonal (bct) geometry. The former ratio, of course, corresponds to the bcc structure. And, as we show in Figure 3, the latter ratio is actually a face centered cubic net.[38] Thus, as might have been anticipated, both the bcc and the fcc structures are global minimum energy structures. There is, however, one interesting finding. For one or another metal structure, bcc and fcc actually correspond to saddlepoints and not minima. Some thought will show there is no straightforward symmetry explanation for this latter finding.

In molecular chemistry such high symmetry saddlepoints are generally associated with the Jahn−Teller effect.[39−41] A well-known example is for Jahn−Teller-unstable octahedral molecules.[42] This is illustrated in Figure 4. Here the octahedron is unstable both with respect to a deformation (e.g. low spin d^7, d^8, and d^9; the figure shows d^7) to a geometry with four short and two long bonds and to the one with two short and four long bonds. These are two phases of an e_g vibration. As in the bcc and fcc cases, the high-symmetry geometry belongs to the O_h point group, the low-symmetry geometry to D_{4h}. This formal analogy is recapitulated in Figure 1.

A question naturally arises: Are the saddlepoints found in Figure 2 due to the solid-state equivalent of the Jahn−Teller effect? This possibility has been mentioned before.[43−46] In this earlier work, particular attention has been paid to how the number of degenerate highest occupied crystal orbitals is significantly reduced in going from the high-symmetry to the low-symmetry structure. Here we are interested instead in applying many of the well-developed orbital concepts from our understanding of the molecular Jahn−Teller effect[40,42] to the question of metal and alloy structure. In this regard, it is known that simple tight-binding or Hückel theory can be used to account for Jahn−Teller instabilities, and that indeed such formalisms often provide the most clear interpretations, capturing the essence of the phenomenon. If this analogy holds, we might expect that a tight-binding calculation will also have an

(25) Todorov, E.; Evans, M.; Lee, S.; Rousseau, R. *Chem.*: *Eur. J.* **2001**, *7*, 2652.
(26) The true TaIr structure is doubly hexagonal closest packed, dhcp, a structure intermediate between fcc and hcp. In Figure 2, however, the only accessed closest packed structure is fcc, a structure whose energy is fairly close to that of dhcp. Hence in this figure fcc appears to be the global minimum.
(27) Sliwko, V. L.; Mohn, P.; Schwarz, K.; Blaha, P. *J. Phys.*: *Condens. Matter* **1996**, *8*, 799.
(28) Sob, M.; Wang, L.; Vitek, V. *Comput. Mater. Sci.* **1997**, *8*, 100.
(29) Watanabe, S.; Komine, T.; Kai, T.; Shiiki, K. *J. Magn. Magn. Mater.* **2000**, *220*, 277.
(30) Suzuki, T.; Shimono, M.; Kajiwara, S. *Mater. Sci. Eng.* **2001**, *A312*, 104.
(31) Friak, M.; Sob, M.; Vitek, V. *Phys. Rev. B* **2001**, *63*, 52405.
(32) Kraft, T.; Marcus, P. M.; Methfessel, M.; Scheffler, M. *Phys. Rev. B* **1993**, *48*, 5886.
(33) Craievich, P. J.; Weinert, M.; Sanchez, J. M.; Watson, R. E. *Phys. Rev. Lett.* **1994**, *72*, 3076.
(34) Alippi, P.; Marcus, P. M.; Schleffer, M. *Phys. Rev. Lett.* **1997**, *78*, 3892.
(35) Tian, Y.; Jona, F.; Marcus, P. M. *Phys. Rev. B* **1998**, *58*, 14051.
(36) Qiu, S. L.; Marcus, P. M.; Ma, H. *J. Appl. Phys.* **2000**, *87*, 5932.
(37) Jona, F.; Marcus, P. M. *Phys. Rev. B* **2001**, *63*, 094113.
(38) This path has a long history in theoretical metallurgy; it goes back to a paper by Bain (see: Bain, E. C. *Trans. AIME* **1924**, *70*, 25).
(39) Jahn, H. A.; Teller, E. *Proc. R. Soc.* **1937**, *A161*, 220.
(40) Bartell, L. S. *J. Chem. Educ.* **1968**, *45*, 754.
(41) Pearson, R. G. *Proc. Natl. Acad. Sci. U.S.A.* **1975**, *72*, 2104.
(42) Burdett, J. K. *Molecular Shapes*: *Theoretical Models of Inorganic Stereochemistry*; J. Wiley: New York, 1980; pp 170−185.
(43) Ashkenazi, J.; Darcorogna, M.; Peter, M.; Talmor, Y.; Walker, E.; Steinemann, S. *Phys. Rev. B* **1978**, *18*, 4120.
(44) Asano, S.; Ishida, S. *J. Phys. Soc. Jpn.* **1985**, *54*, 4241.
(45) Fujii, S.; Ishida, S.; Asano, S. *J. Phys. Soc. Jpn.* **1989**, *58*, 3657.
(46) Sakuma, A.; Yuasa, S.; Miyajima, H.; Otani, Y. *J. Phys. Soc. Jpn.* **1995**, *64*, 4914.

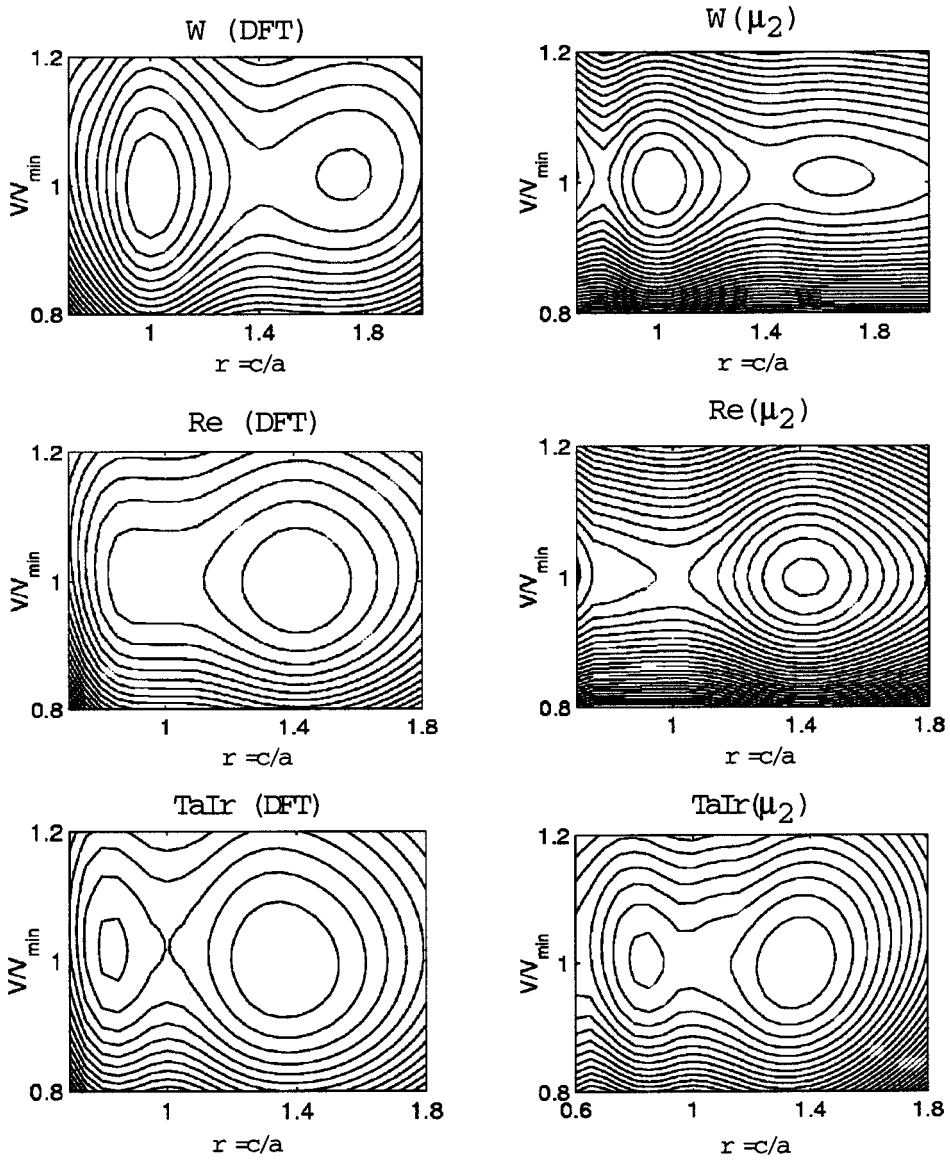

Figure 2. Contour energy surfaces for W, Re, and TaIr with LDA-DFT and the μ_2-Hückel method.[25]

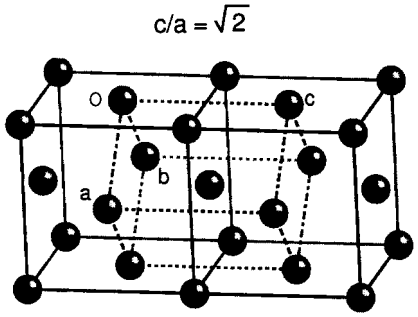

Figure 3. Equivalence of $c/a = \sqrt{2}$ bct and fcc structure.

energy surface similar to the DFT surface. The actual method we choose to use is the μ_2-Hückel method,[47−58] a tight-binding one-electron calculation where a pairwise repulsive energy is added to the attractive Hückel energy. In Figure 2b,d we show the results of a μ_2-Hückel tight-binding calculation for W, Re, and TaIr. It can be seen that the one-electron calculations capture the essential energetics of the three systems, both in the location of the energy minima and the energy saddlepoints.[59] Encouraged by these findings, we turn to developing an orbital-based tight-binding model for the stability of elemental metal and alloy structures.[60]

(47) Pettifor, D. G.; Podloucky, R. *Phys. Rev. Lett.* **1984**, *53*, 1080.
(48) Pettifor, D. G. *Solid State Phys.* **1987**, *40*, 43.
(49) Lee, S. *Acc. Chem. Res.* **1991**, *24*, 249.
(50) Lee, S. *J. Am. Chem. Soc.* **1991**, *113*, 101.
(51) Cressoni, J. C.; Pettifor, D. G. *J. Phys.: Cond. Matter* **1991**, *3*, 495.
(52) Lee, S.; Foran, B. *J. Am. Chem. Soc.* **1994**, *116*, 154.
(53) Lee, S.; Hoistad, L. *J. Alloys Comput.* **1995**, *229*, 66.
(54) Häusermann, U.; Nesper, R. *J. Alloys Comput.* **1995**, *218*, 244.
(55) Gweon, G. H.; Denlinger, J. D.; Clack, J. A.; Allen, J. W.; Olson, C. G.; DiMasi, E.; Aronson, M. C.; Foran, B.; Lee, S. *Phys. Rev. Lett.* **1998**, *81*, 886.
(56) Rousseau, R.; Tse, J. S. *Prog. Theor. Phys. Suppl.* **2000**, *138*, 47.
(57) Tse, J. S.; Uehara, K.; Rousseau, R.; Ker, A.; Ratcliffe, C. I.; White, M. A.; Mackay, G. *Phys. Rev. Lett.* **2000**, *85*, 114.
(58) Tse, J. S.; Frapper, G.; Ker, A.; Rousseau, R.; Klug, D. D. *Phys. Rev. Lett.* **1999**, *82*, 4472.
(59) In the μ_2-Hückel energy surfaces of Figure 2, one can see the onset of an additional energy minimum at low values of c/a. The source for this error is well understood. The μ_2-Hückel Hamiltonian is most accurate when comparing structures with reasonably similar coordination numbers. It has been proven to give qualitative and semiquantitative energies when contrasting one alloy structure with another. Therefore in Figure 2, it is not useful when comparing the two-coordinate linear chain structure found for $c/a = 0.6$ to the twelve- or fourteen-coordinate fcc and bcc structures found at $c/a = 1.4$ and 1.0.

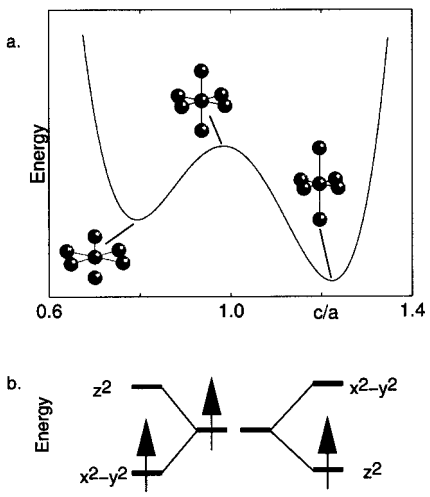

Figure 4. Jahn−Teller energetics for an octahedral molecule. The e_g level is shown, with an electron occupation corresponding to d^7.

Calculational Methods

Local density approximation (LDA) DFT calculations were carried out with the Vienna Ab Initio Simulation Package (VASP),[61−64] using the ultrasoft Vanderbilt pseudopotentials[65] provided by the package. Plane wave basis sets were used in the high precision mode. This corresponds to plane wave energy cutoffs of 218.3, 235.3, and 247.8 eV for respectively Ta, W, and Ir. The Brillouin zone sampling was done by the Monkhost-Pack[66] **k** points grid (15 × 15 × 15 mesh). Partial occupancies of wave functions were made based on the tetrahedron method with Blöchl correction.[67]

The μ_2-Hückel method[23,47−58] is based on a tight-binding approach,[12−15,68−76] where we express the total energy, E_T, as

$$E_T(r) = U(r) - V(r)$$

where $U(r)$ is a hard-core interatomic repulsion energy, $V(r)$ is an attractive bonding energy, and r is a parameter dependent on the size of the system. The total energy E_T can be expressed as

$$E_T = \gamma \int_{-\infty}^{\infty} (E - E_{avg})^2 \rho(E\,r)\,dE + \int_{-\infty}^{E_F} E\rho(E\,r)\,dE$$

where the integrals represent respectively the repulsive and the attractive energy. Here $\rho(E,r)$ is the electronic density of states, E_F is the Fermi energy, E_{avg} is the average energy of the electronic density of states, and γ is a proportionality constant. The density $\rho(E,r)$ is found from the diagonalization of the Hamilton matrix. Diagonal elements, H_{ii}, are set equal to prescribed Coulombic integral values, while off-diagonal elements are based on the Wolfsberg−Helmholz approximation,[77] $H_{ij} = {}^1/_2 KS_{ij}(H_{ii} + H_{jj})$. The parameter K is generally set to 1.75 and S_{ij} is the overlap integral between the atomic orbitals i and j. Atomic orbitals are assumed to be single or double ζ expansion Slater-type orbitals.

For the elemental systems the atomic parameters are the same ones used effectively in previous work on transition metal alloys and main group systems.[78,79] Since the only previous transition metal μ_2-Hückel parameters developed have been for first row elements, we used these parameters again here: $H_{ii}(4s) = -9.10$ eV, $H_{ii}(4p) = -5.32$ eV, $H_{ii}(3d) = -12.60$ eV; $\zeta(4s) = \zeta(4p) = 1.9$, $\zeta_1(3d) = 5.35$ (0.5505), $\zeta_2(3d) = 2.00$ (0.6260). In the case of TaIr it has been determined that the difference of energy in the *d*-orbitals is approximately 6 eV,[80] and therefore the Ir Coulombic integrals were placed 6 eV lower than their Ta counterparts. However, within a single element the difference between the *s*, *p*, and *d* orbitals was maintained as above. Thus Ir *s*, *p*, and *d* Coulombic integrals were set at −14.45, −10.95, −7.17 eV and their Ta counterparts were at −8.45, −4.95, −1.17 eV. Slater exponents were also left unchanged. In the case of Ge $H_{ii}(4p) = -9.00$ eV and $\zeta(4p) = 1.85$ (the reason for introducing this main group element will be given below). While our choice of parameters might seem arbitrary, it meets the criteria of what we want—a minimally complicated model that allows for both electron count differences and ionicity.

The parameter γ was determined from the condition that the total energy, E_T, should be a global energy minimum for bcc and fcc cells with the sizes stipulated below. For calculating μ_2-Hückel energies either a 900 special point[81] rectangular mesh or a 1000 special point orthorhombic mesh was used. For calculating ΔE_{star} (to be defined below) we used a 101 × 101 *k*-mesh for two-dimensional systems and a 51 × 51 × 51 mesh for three-dimensional systems. For Figure 2, we considered all overlap interactions between atoms less than 10 Å apart. For all other tight-binding calculations we considered overlaps between atoms less than 3.1 Å apart. This lower value limits the overlaps to first nearest neighbors for the square net and fcc and to first or second nearest neighbors for bcc.

As will be shown in the text, ΔE_{star} is almost nondifferentiable near the Fermi surface. This is especially true for the perfectly square or cubic structures. We distorted slightly the high-symmetry cubic cells to alleviate this problem. For the three systems so studied, square vs rectangular, bcc vs bct, and fcc vs fct, we shifted the cell axis ratios to be respectively 1.008, 1.010, and 0.992. For the results of Figures 10, 12, and 16 we made these same shifts in the corresponding μ_2-Hückel calculations. Thus for these figures we used for a square net a 2.39 × 2.41 Å cell, for the rectangular net a 2.38 × 2.42 Å cell, for bcc a 2.87 × 2.87 × 2.90 Å cell, for bct a 2.86 × 2.86 × 2.92 Å cell, for fcc a 3.59 × 3.59 × 3.56 Å cell, and for fct a 3.60 × 3.60 × 3.54 Å cell. For Figure 11 we use two equivalent density cells with $a = 2.88$ Å for bcc and $a = 3.628$ Å for fcc. The band diagrams in Figure 14 are for an $a = 2.88$ Å bcc cell, and a 2.86 × 2.86 × 2.934 Å bct cell. In Figure 18 the fcc cell has $a = 3.56$ Å and the fct cell is 3.60 × 3.60 × 3.48 Å. As energies near saddlepoints and minima are dominated by the quadratic term in their Taylor expansion, we can estimate the error introduced by these slight misrepresentations of the square, bcc, and fcc structures. In Figures 10, 12, and 16 the differences in energy are roughly 25% too small. This in no way affects the qualitative understanding derived from these calculations.

Discussion

Jahn−Teller Effect for a Solid. Static molecular Jahn−Teller distortions are caused by strong electronic-vibrational

(60) There are alternate tight-binding approaches where one does not as explicitly consider the symmetry-adapted crystal orbitals when accounting for structural distortions. One such approach uses the various moments of the electronic density of states. In a classic illustration of this theory,[11] it has been shown that the fourth moment of the bcc structure is much less than that of fcc and that this difference can account for the difference in energies between these two structures. In this article we consider directly the symmetry-adapted crystal orbitals and do not apply such moment-based analyses.

(61) Kresse, G.; Hafner, J. *Phys. Rev. B* **1993**, *47*, 55.
(62) Kresse, G.; Hafner, J. *Phys. Rev. B* **1994**, *49*, 14251.
(63) Kresse, G.; Furthmüller, J. *Comput. Mater. Sci.* **1995**, *6*, 15.
(64) Kresse, G.; Furthmüller, J. *Phys. Rev. B* **1996**, *54*, 11169.
(65) Vanderbilt, D. *Phys. Rev. B* **1990**, *41*, 7892.
(66) Monkhost, H. J.; Pack, J. F. *Phys. Rev. B* **1976**, *13*, 5188.
(67) Blöchl, P. E.; Jepsen, O.; Andersen, O. K. *Phys. Rev. B* **1994**, *49*, 16223.
(68) Cohen, R. E.; Mehl, M. J.; Papaconstantopoulos, D. A. *Phys. Rev. B* **1994**, *50*, 14694.
(69) Mehl, M. J.; Papaconstantopoulos, D. A. *Phys. Rev. B* **1996**, *54*, 4519.
(70) Cerdá, J.; Soria, F. *Phys. Rev. B* **2000**, *61*, 7965.
(71) Foulkes, W. M. C.; Haydock, R. *Phys. Rev. B* **1989**, *39*, 12520.
(72) Cohen, R. E.; Stixrude, L.; Wasserman, E. *Phys. Rev. B* **1997**, *56*, 8575.
(73) Ordejón, P. *Comput. Mater. Sci.* **1998**, *12*, 157.
(74) Ortega, J. *Comput. Mater. Sci.* **1998**, *12*, 192.
(75) Frauenheim, T.; Seifert, G.; Elstner, M.; Hainal, S.; Jungnickel, G.; Porezag, D.; Suhai, S.; Scholz, R. *Phys. Stat. Sol. B* **2000**, *217*, 41.
(76) Elstner, M.; Frauenheim, T.; Kaxiras, E.; Seifert, G.; Suhai, S. *Phys. Stat. Sol. B* **2000**, *217*, 357.
(77) Wolfsberg, M.; Helmholz, L. *J. Chem. Phys.* **1952**, *20*, 837.
(78) Summerville, R. H.; Hoffmann, R. *J. Am. Chem. Soc.* **1976**, *98*, 7240.
(79) Hoistad, L. M.; Lee, S. *J. Am. Chem. Soc.* **1991**, *113*, 8216.
(80) Pyykkö, P.; Lohr, L. L. *Inorg. Chem.* **1981**, *20*, 1950.
(81) Chadi, D. J.; Cohen, M. L. *Phys. Rev.* **1973**, *B8*,.

coupling. There are several equivalent ways to describe what transpires; the one we choose is an orbital-based description. In this language, the Jahn−Teller phenomenon is characteristic of a set of partially occupied highest occupied molecular orbitals (HOMO). In general these energetically degenerate HOMOs belong to the same irreducible representation of the molecular symmetry group. The distortion (an excursion along a normal mode) lifts the degeneracy. Solid-state equivalents of the Jahn−Teller effect are well-known. The best studied are the Peierls distortion[82] and charge density waves (CDW).[83−85] There is, however, one notable difference between the molecular Jahn−Teller effect and the Peierls or CDW distortion. *In the former case the lost symmetry element is a point group operation*; *in the latter it is a translation*. In the bcc, fcc, and bct cells, while the conventional crystallographic cells have more than one atom, the primitive cells all have only one atom each. Hence in going from bcc to bct to fcc, there is no loss of translational symmetry. To analyze the effect of change of symmetry on these systems we must turn to the full space group of the crystal and not just its translational portion.

We recall that a crystal orbital is a Bloch function: $\Phi_{\vec{k}} = (1/\sqrt{N})\sum e^{i\vec{k}\cdot\vec{r}_j}\,\phi_j$, where $\vec{k}$ is the *k*-vector, $\vec{r}_j$ the atomic positions, and ϕ_j the atomic orbitals. If we now apply a point group operation of the crystal, *R*, to this Bloch function, we find:

$$R\Phi_{\vec{k}} = R\left\{\frac{1}{\sqrt{N}}\sum e^{i\vec{k}\cdot\vec{r}_j}\,\phi_j\right\} = \frac{1}{\sqrt{N}}\sum e^{i\vec{k}\cdot R\vec{r}_j}\,R\phi_j = \frac{1}{\sqrt{N}}\sum e^{i\vec{k}\cdot R\vec{r}_j}\,\phi_j = \frac{1}{\sqrt{N}}\sum e^{iR^{-1}\vec{k}\cdot\vec{r}_j}\,\phi_j = \Phi_{R^{-1}\vec{k}}$$

In the penultimate equality we use the fact that a dot product is proportional to the angle between two vectors; thus if one rotates just one of the two vectors in the dot product as in $\vec{k}\cdot R\vec{r}_j$ this is equivalent to rotating the other vector in the dot product by an equal and opposite rotation as in $R^{-1}\vec{k}\cdot\vec{r}_j$.

As the above expressions demonstrate the equality of $R\Phi_{\vec{k}}$ and $\Phi_{R^{-1}\vec{k}}$, the point group operation maps $\Phi_{\vec{k}}$ onto $\Phi_{R^{-1}\vec{k}}$, and hence these two Bloch functions belong to the same irreducible representation. Furthermore, by definition, R^{-1} is also an element of the same point group. It is conventional to call the set of vectors $\{R\vec{k}\}$, where *R* is any point group operation component of a space group element, a star of reciprocal vectors, or k_{star}.[86]

A Two-Dimensional Model. We now consider how k_{star} can help in the analysis of a Jahn−Teller distortion in a solid, i.e. a distortion in which the point group portion of the space group is changed but where the translational portion remains unaffected. To understand the situation we need to go back to a simpler model than our three-dimensional lattice, yet one which captures the physical essence of the phenomenon. In this spirit, consider a simple square net of germanium atoms that undergoes a distortion to a simple rectangular net. This distortion is illustrated in Figure 5. For the sake of simplicity we restrict the valence orbitals to the *p*-manifold and assume (in the spirit of a Hückel model) that there is interaction between nearest neighbors only. In such a case there is no mixing between the

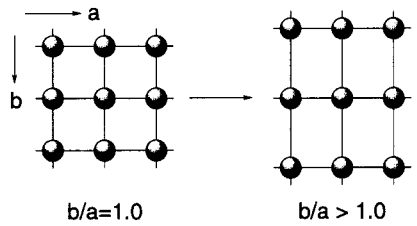

Figure 5. Distortion of a square to a rectangular net.

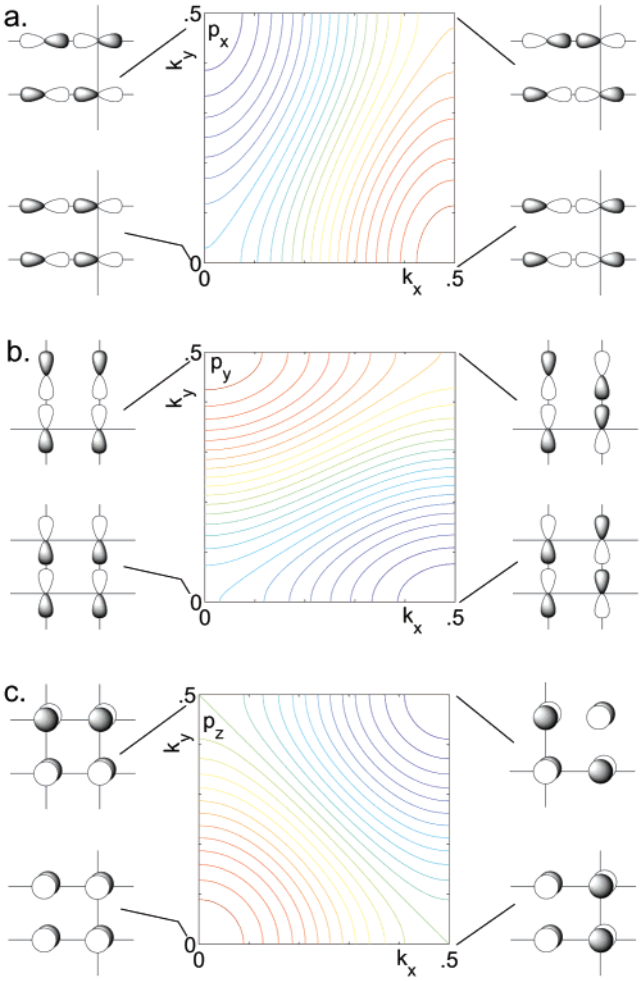

Figure 6. Energy contour map of square net p_x, p_y, and p_z orbitals. Energies are color coded. Red corresponds to bonding, green to nonbonding, and blue to antibonding.

p_x, p_y, and p_z sets. The energies of the Bloch crystal orbitals are illustrated in Figure 6. These energies are simply understood. For example, for p_x the lowest energy orbital is at $\vec{k} = (1/2, 0)$ and the highest energy orbital is at $\vec{k} = (0, 1/2)$ as these orbitals are respectively purely bonding (σ and π) and purely antibonding. Similarly, at these same $\vec{k}$-vectors, the p_z orbitals are nonbonding.

In the undistorted square net a 90° rotation is a symmetry operation, and $\vec{k} = (1/2, 0)$ and $\vec{k} = (0, 1/2)$ belong to the same k_{star}. Thus, the p_z based crystal orbitals at these two *k*-points belong to the same irreducible representation. But for the rectangular net a 90° rotation is not a symmetry operation, and these two orbitals are no longer degenerate. This is shown in Figure 7a. If we assume a band-filling of three electrons per atom (e^-/a) the p_x, p_y, and p_z are each filled with a single

(82) Peierls, R. E. *Quantum Theory of Solids*; Clarendon Press: Oxford, 1955.
(83) Wilson, J. A.; DiSalvo, F. J.; Mahajan, S. *Adv. Phys.* **1975**, *24*, 117.
(84) Monceau, P.; Ong, N. P.; Portis, A. M.; Meerschaut, A. M.; Rouxel, J. *Phys. Rev. Lett.* **1976**, *37*, 602.
(85) Canadell, E.; Whangbo, M. H. *Chem. Rev.* **1991**, *91*, 965.
(86) Lax, M. *Symmetry Principles in Solid State and Molecular Physics*; J. Wiley: New York, 1974.

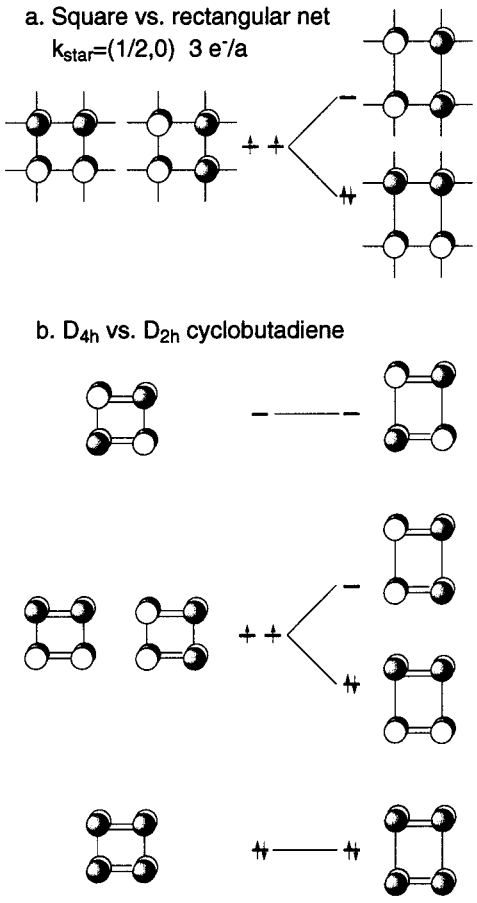

Figure 7. Effect of rectangular distortion (a) on the p_z $\vec{k} = (0, 1/2)$ and $\vec{k} = (1/2, 0)$ orbitals of a square net for a band filling of 3 electrons per atom and (b) for the π-orbitals of cyclobutadiene.

electron, all bonding orbitals are filled, and all nonbonding orbitals are half-filled. For this number of electrons, Figure 7a begins to resemble a conventional diagram for the molecular Jahn−Teller effect. Thus at 3.0 e$^-$/a, there may be a Jahn−Teller effect stabilizing the rectangular geometry.

The picture in Figure 7a is thus reminiscent of the classic molecular Jahn−Teller system, cyclobutadiene. In cyclobutadiene there are four π molecular orbitals (Figure 7b) and four π-electrons. The shape of these π-orbitals is completely determined by symmetry. Were cyclobutadiene to adopt a square geometry there would be one bonding, one antibonding, and two nonbonding π-orbitals. In a square geometry these two nonbonding orbitals are degenerate and half-filled. Under a distortion from D_{4h} to D_{2h} symmetry this pair of orbitals splits into two: one orbital becomes weakly bonding, the other antibonding. The classic rationalization for why cyclobutadiene has a D_{2h} ground-state geometry is that in this latter geometry all the π-electrons are in bonding orbitals.[3]

The strong similarity between the square and rectangular net orbitals shown in Figure 7a and the cyclobutadiene orbitals shown in the center of Figure 7b suggests a strategy to quantify potential Jahn−Teller effects in extended solids. It is one which retains, as much as possible, the feel of molecular Jahn−Teller theory. In Figure 7, we saw for both molecule and extended net the driving force for distortion is a pair of orbitals which are degenerate in the high-symmetry geometry but have different energies in the low-symmetry structure. In the cases shown in Figure 7, this distortion is further abetted by electron transfer between the formerly degenerate orbitals, from the situation where both orbitals are filled by one electron to the one where one orbital is empty, the other filled.

In studying extended solids, we therefore focus on orbitals which by symmetry are degenerate in the high-symmetry structure but are not degenerate in the low-symmetry structure. As in Figure 7, we restrict ourselves to electron transfer between these symmetry related orbitals. In the language of the solid state, we restrict electron transfer to that between two $\vec{k}$-vectors belonging to the same k_{star} (see above). We keep the number of electrons in each k_{star} fixed and calculate for each k_{star} the difference in energy between the undistorted and distorted geometry. The number of electrons in each k_{star} is set equal to that found in the undistorted structure. We call this energy $\Delta E_{star}(\vec{k})$ or just ΔE_{star}. The total difference in energy can be obtained by integrating this function.

In considering this ΔE_{star} function, we make the assumption that it is the interplay between crystal orbitals which are related to one another by symmetry that plays a central role in the Jahn−Teller energetics, rather than crystal orbitals which are just accidentally degenerate. This is a strong assumption, as in metals there is in general a two-dimensional surface of states which are accidently degenerate. Indeed, it is known that such accidental degeneracies can play a considerable role in metal and alloy phonon structure.[43,87,88]

In Figure 8 we show this ΔE_{star} function for two different bandfillings, 1.2 and 3.0 e$^-$/a (electrons per atom). (We choose these two band fillings for as we show below, they correspond to the electron counts where there are cusps in ΔE_{star}.) For both, the ΔE_{star} is nearly zero, except at several well-defined k_{star}. As may be seen in Figure 8, these peaks have the form of ridges.

It is especially instructive to compare these ridges with the contour maps of the p crystal orbitals, shown previously in Figure 6. In particular, we need to concentrate on the contour lines in Figure 6 which correspond to the highest occupied molecular orbitals, i.e. the orbitals at the Fermi energy. Consider first 3.0 e$^-$/a, where the p_x, p_y, and p_z orbitals are all half-filled. For this case, the contour lines which correspond to the highest occupied molecular orbitals are purely nonbonding. They are the pure green lines of Figure 6 and they are only partially filled with electrons. For the p_z crystal orbitals, these nonbonding molecular orbitals correspond to the straight contour line that runs from the upper left of Figure 6c to the lower right.

When one compares the green contour lines of Figure 6 with the ΔE_{star} function for 3.0 e$^-$/a, shown in Figure 8, we see something interesting. The ridges in the ΔE_{star} function are at exactly the same location as the green contour lines. Why should such a correspondence exist? Recall that at 3.0 e$^-$/a the green contour lines indicate those orbitals which are only partially filled with electrons. Recall also that the ΔE_{star} function groups together the orbitals which are related to one another by symmetry. The correspondence of the contour lines and the ridges of the ΔE_{star} function tell us that both partial orbital occupation and the grouping together of symmetry equivalent orbitals are important.

To understand why this is so, consider again cyclobutadiene (see Figure 7b). In cyclobutadiene's square geometry there are

(87) Varma, C. M.; Weber, W. *Phys. Rev. B* **1979**, *19*, 6142.
(88) Herper, H. C.; Hoffmann, E.; Entel, P.; Weber, W. *J. Phys. IV* **1995**, *5*, C8−293.

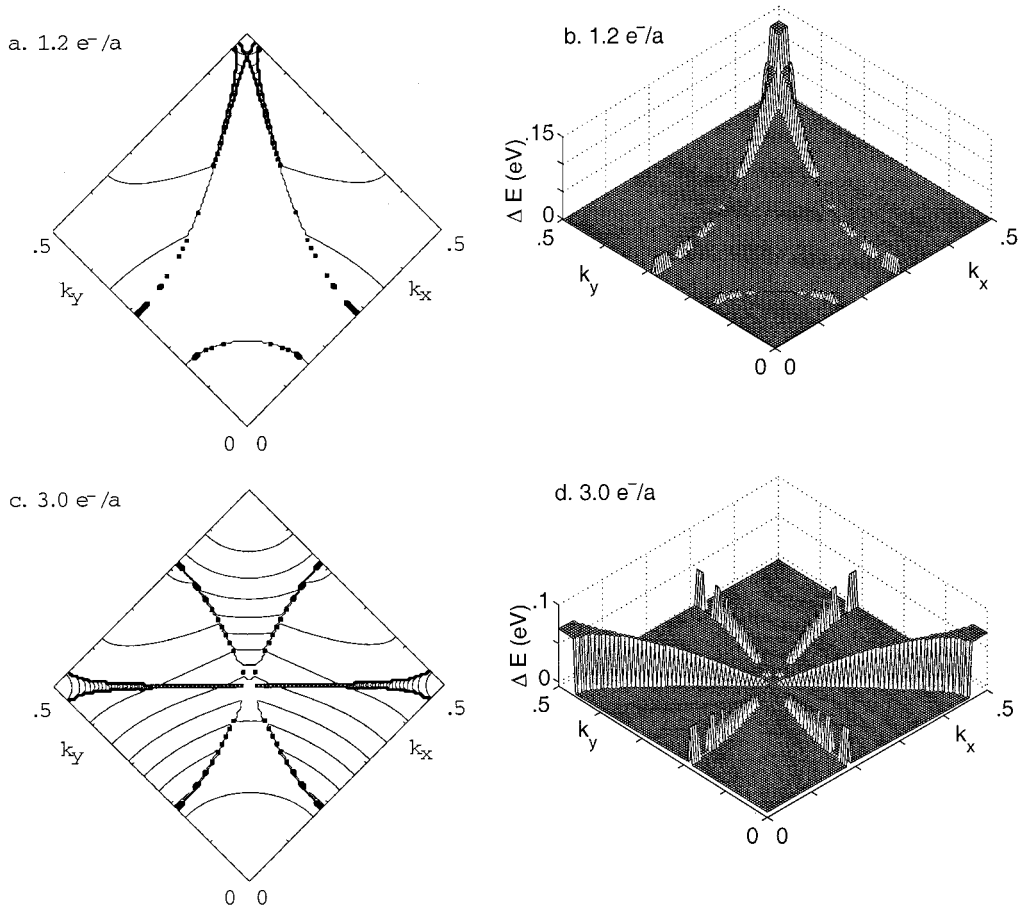

Figure 8. ΔE_{star} for a square vs a rectangular net: (a and b) at 1.2 and (c and d) at 3.0 e^-/a.

two *partially filled symmetry-related* nonbonding orbitals. Under the rectangular distortion they split apart in energy: one orbital becoming slightly bonding and the other slightly antibonding. Given the initial partial occupation of these two orbitals by just two electrons, the slightly bonding orbital is filled and the slightly antibonding orbital is unfilled: the system is stabilized.

For the same phenomenon to occur in the solid state, just as in cyclobutadiene, one needs again partially filled symmetry-related orbitals. There must be a set of originally degenerate orbitals which are energetically split apart by the distortion: some going down in energy and others going up in energy. This set of orbitals must be partially filled so that the energy stabilization found from the set of stabilized orbitals is not counteracted by occupation of the others. In the case of the square to rectangle distortion for 3.0 e^-/a, the partially filled orbitals are the orbitals which correspond to the green contour lines in Figure 6. The symmetry-related degenerate orbitals correspond to the individual k_{star}. Hence it is only these green contour orbitals and their k_{star} related orbitals that cause the solid-state Jahn−Teller distortion.

However, Figure 8 also shows that not all Fermi surface states contribute equally to ΔE_{star} (in a metal the HOMO orbitals are said to be on the Fermi surface). At 1.2 e^-/a, the ridge in the ΔE_{star} function is highest where k_{star} is ($^1/_2$, $^1/_2$) while at 3.0 e^-/a, the ridge is highest at ($^1/_2$, 0). Actually, these band fillings are not just pedagogical examples—we have surveyed the full range of electron populations and these two band-fillings are those with the largest values of ΔE_{star}. It should be noted though the square net is alternant (by alternant we mean there are no odd member rings of bonded atoms).[89] At the Hückel level, this results in a pairing of filled and unfilled levels; thus ΔE_{star} at 4.8 e^-/a (1.2 holes per atom) is by symmetry the same as that at 1.2 e^-/a.

The explanation for the relative heights of these ridges may be found by examining the *shape* of the orbitals in the k_{star} themselves. We consider first the 1.2 e^-/a system. At $\vec{k} = (^1/_2, ^1/_2)$, the two energetically degenerate Fermi surface orbitals are the p_x and p_y orbitals. The p_x orbital, shown at the left of Figure 9, is σ-bonding in the horizontal direction, but π-antibonding in the vertical direction. The converse is true for the p_y orbital. Under the rectangular distortion, horizontal interactions become stronger and vertical interactions weaker. As the p_x orbital is bonding in one direction and antibonding in the other, such a distortion causes a large decrease in crystal orbital energy; similarly, the p_y orbital increases in energy. The result is a large driving force for the Jahn−Teller effect associated with this pair of orbitals at this particular electron count.

For 3.0 e^-/a the most energetically important orbitals are the p_z orbitals at $\vec{k} = (^1/_2, 0)$ and $(0, ^1/_2)$. These were shown in Figure 7a. One member of this pair of orbitals is bonding in the horizontal direction and antibonding in the vertical direction, while the opposite is true for its partner orbital. Again, the result is a large associated Jahn−Teller effect.

(89) Coulson, C. A.; Rushbrooke, G. S. *Proc. Cambridge Philos. Soc.* **1940**, *36*, 193.

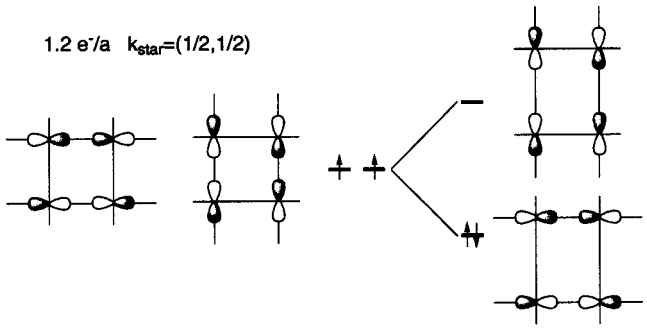

Figure 9. Effect of rectangular distortion of a square net on the p_x and p_y $\vec{k} = (1/2, 1/2)$ orbitals for a band filling of 1.2 electrons per atom.

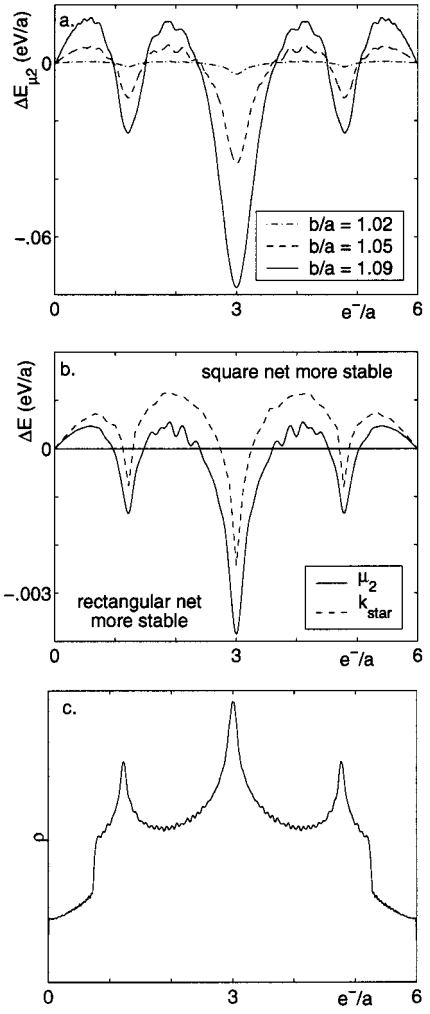

Figure 10. (a) Difference in μ_2-Hückel energies between the square net and a rectangular net. Negative values correspond to the rectangular net being more stable. (b) Comparison of ΔE_{star} and $\Delta E_{\mu 2}$ for the square vs rectangular ($b/a = 1.02$) net. Note the ΔE-scale is different from Figure 10a. (c) The square net electronic density of states as a function of band filling.

ΔE_{star} is also useful in analyzing the total difference in energy. In Figure 10a, we show the results of a μ_2-Hückel calculation for the square and rectangular net. Plotted is the difference in energy between these two structures, $\Delta E_{\mu 2}$, as a function of band filling. The curves are plotted so that a positive value corresponds to the square net being more stable and a negative value to the rectangular net being more stable. It can be seen that near 1.2, 3.0, and 4.8 e^-/a, the rectangular structure is preferred. These are exactly the electron counts discussed in the preceding paragraphs. As Figure 10a shows, the magnitude of this difference in energy is controlled by the size of the distortion. As the square net ($b/a = 1.0$) is an energetic saddlepoint, we expect that the quadratic term will dominate a Taylor series expansion around the saddlepoint geometry. This quadratic relation roughly holds between $b/a = 1.02$ and 1.05, but is less correct at higher b/a values.

In Figure 10b, we compare directly $\Delta E_{\mu 2}$ with ΔE_{star} for $b/a = 1.02$, where we have integrated the latter function over k-space.[90] It can be seen that the two functions are quite similar. Both functions have sharp spikes near 1.2, 3.0, and 4.8 e^-/a. The functions differ by an approximately parabolic function that is greatest at the half-filled band and zero at the band edges. Such an error is expected, as we have not made an interatomic repulsion correction in ΔE_{star} but have in $\Delta E_{\mu 2}$. Such a correction is expected to be parabolic.[23]

Finally, in Figure 10c we compare these difference in energy curves with the electronic density of states (DOS). It is conventional to plot the DOS as a function of the Fermi energy. Here we plot the DOS as a function of band-filling. In this way we can directly compare parts b and c in Figure 10. We see that the band fillings with the largest Fermi surface, i.e. the greatest number of highest occupied molecular orbital states, are the same band fillings for which the Jahn−Teller distortion is strongest. The shape of the density of states can be understood by reexamining Figure 6. It is precisely at these electron concentrations where the contour lines intersect the corners of the diagrams. These corners are high symmetry points in k-space, where bands in the band diagram have zero slope.[91] Therefore, it is at these electron counts where not only the Fermi surface contour lines are longest, but also the Fermi surface contour slopes are flattest. Consequently it is at these k-points where the electronic density of states is highest.

However, our preceding analysis at 1.2 and 3.0 e^-/a shows that this correspondence is somewhat misleading. As we discussed earlier, it is not the length or width of the ridges in ΔE_{star} which are important, rather it is the magnitude of the major peaks in these ridges. A similar phenomenon is found for molecular Jahn−Teller distortions. For example, in transition metal octahedral complexes there are three t_{2g} orbitals and only two e_g orbitals, but it is the e_g-based Jahn−Teller instabilities which have the greatest distortions.[42] The reason for this is clear—the e_g levels are σ-antibonding, the t_{2g} levels σ-nonbonding (or π-antibonding if the ligands are π donors).

If it is a coincidence that the electron fillings with the largest electronic density of states are also the ones where ΔE_{star} has its largest values, what is the reason for it? Again we turn to Figure 6. It is the orbitals at the corners of the diagrams in Figure 6 that are maximally bonding and antibonding. And more to the point, it is at the corners where orbitals are maximally bonding along one axis direction and antibonding along the other. ΔE_{star} is therefore maximized when these corner orbitals lie on the Fermi surface. Similarly it is the contours which pass through these same corner states which are both flattest and

(90) We choose such a small distortion as the interest in this paper is the Jahn−Teller distortion itself and hence the energetic behavior near the high-symmetry structure.
(91) Ashcroft, N. W.; Mermin, N. D. *Solid State Physics*; Holt, Rinehart and Winston: New York, 1976; p 145.

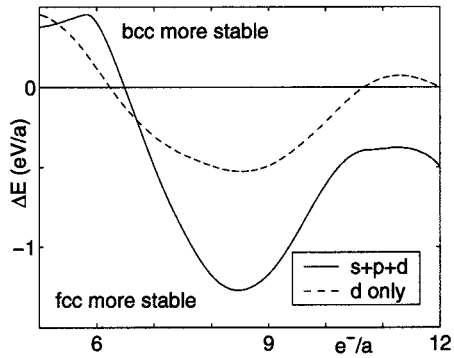

Figure 11. Difference in μ_2-Hückel energies between bcc and fcc. Negative values correspond to the fcc being more stable. In the *d*-only model, the *d*-band electron concentration is multiplied by $^6/_5$ to simulate partial *s*-band fillings.

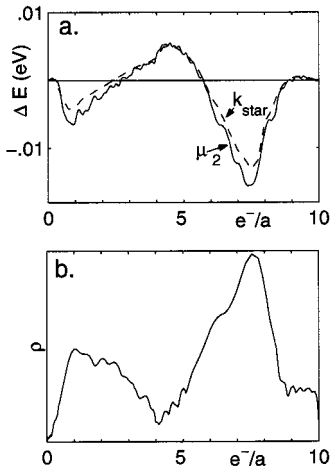

Figure 12. (a) Difference in energies between bcc and bct ($c/a = 1.02$) using a *d*-orbital only model. Negative values correspond to bct being more stable. Differences in energy are per atom. (b) Electronic density of states for bcc given as a function of *d*-orbital band-filling.

longest; this is where one finds the greatest values of the electronic density of states.

Thus the corners in Figure 6 determine both the maximum values of ΔE_{star} *and* the maxima in the density of states. This accounts for the agreement between parts b and c in Figure 10. We note that $\vec{k}$-vectors such as Γ, ($^1/_2$, 0), (0, $^1/_2$), and ($^1/_2$, $^1/_2$) are often the places where orbitals are maximally bonding or antibonding. This is especially true for simple systems. Thus although it is a coincidence that there is a correlation between ΔE_{star} and the density of states, it is a coincidence that will frequently occur.

With the experience gained from this two-dimensional problem, we are ready to apply the ΔE_{star} analysis to the three-dimensional problems of central interest to us, the structure of metals and alloys.

Bcc to Bct Distortion. Group 3 and 4 transition metal elements adopt the hcp structure, group 5 and 6 elements the bcc structure, nonmagnetic group 7 and 8 elements the hcp structure, and nonmagnetic group 9−11 elements the fcc structure.[92] In accounting for these facts it is clear that the valence *s*-, *p*-, and *d*-orbitals can all potentially play a role. However, it is well established that it is the *d*-orbitals which are most important. Thus Pettifor has used a near neighbor *d*-orbital model to correctly determine differences in energy between the bcc, fcc, and hcp systems.[93] His results agree with the above experimental findings with one exception: near the completely filled *d*-band, Pettifor's calculations suggest that bcc is preferred over fcc.

In Figure 11 we present the results of μ_2-Hückel calculations comparing the fcc and bcc structures. Two different models are presented. In the first, a full set of *s*-, *p*-, and *d*-orbitals is considered, while in the second only *d*-orbitals are used. To directly compare these calculations we need to assign the occupancy of the *s*- and *p*-bands in the *d*-orbital model. We do so by making the simple assumption that the *p*-band remains unfilled and that the *s*-band occupation is proportional to the *d*-band occupation. We therefore multiply the *d*-band electron concentration by $^6/_5$ to determine the appropriate e$^-$/a level. As Figure 11 shows, the two models are comparable. However, near the filled *s*- and *d*-band limit, the *d*-orbital model has bcc too stable with respect to fcc. This is the same error as found in the Pettifor results. It suggests that for such late transition metal elements *s*- and *p*-orbital effects must be explicitly considered.

In the systems shown in Figure 2, the average electron concentrations are 6 e$^-$/a while for Re and TaIr the concentration is 7 e$^-$/a. At such lower electron counts, a *d*-orbital model captures the principal energetic features. As our goal is to explain, using the simplest picture possible, the energetics of these lower electron count systems, we consider here, as had Pettifor, near neighbor *d*-orbital interactions alone.

We consider first the stability of the bcc net with respect to a bct distortion ($c/a = 1.02$), see Figure 1i. We show the results of both a μ_2-Hückel calculation and an integrated ΔE_{star} function for such a distortion in Figure 12a. As can be seen, the two functions closely track one another. The bcc undistorted structure is preferred near 5 *d*-electrons per atom, but from 6 to 9 *d*-electrons per atom the bct distortion is lower in energy. Recalling the approximate factor of $^6/_5$ necessary to convert these band-fillings to periodic table group numbers, these results suggest that group 5 and 6 transtion metal elements in the bcc structure are not Jahn−Teller unstable, but that group 7 and above elements are Jahn−Teller unstable. This is borne out experimentally. All nonmagnetic transition metal elements belonging to group 7 or higher or group 4 and lower adopt closest packed structures, while group 5 and 6 elements adopt the bcc structure. These results cannot be used to distinguish the fcc from the hcp structures,[94] but as fcc and hcp are structurally similar, the differences in energy between them are small when compared to their differences in energy with respect to the bcc structure. We can therefore assume that the hcp vs bcc energies are fairly similar to the ones shown in Figure 12. That this is so is verified by Pettifor's original results on the fcc, hcp, and bcc structures. In his work, the differences in energy between fcc and bcc were five times greater than those between fcc and hcp.

We can compare these energy difference curves to the electronic density of states plotted as a function of electron

(92) Massalski, T. B.; Okamoto, H.; Subramanian, P. R., Eds. *Binary Alloy Phase Diagrams*, 2nd ed.; American Society for Metals: Metal Park, OH, 1990.
(93) Pettifor, D. G. *Bonding and Structure of Molecules and Solids*; Oxford Science: Oxford, England, 1995; pp 223−226.
(94) Hcp has two atoms in its primitive cell. Hence any study comparing Jahn−Teller instabilities of fcc with respect to hcp requires the use of both rotational and translational symmetry elements, a study outside the compass of the present work.

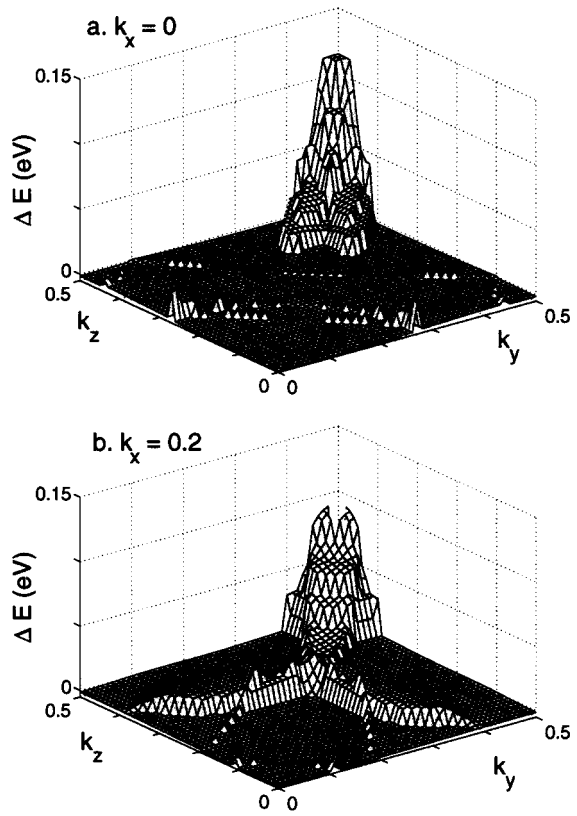

Figure 13. ΔE_{star} for 7.8 e^-/a for bcc and bct ($c/a = 1.02$) using a *d*-orbital only model for (a) $\vec{k} = (0, k_y, k_z)$ and (b) $\vec{k} = (0.2, k_y, k_z)$.

concentration. This latter curve is shown in Figure 12b. As in the case of the square to rectangular distortion discussed previously, there is a coincidence between the electron counts which are Jahn−Teller unstable and the electron counts which have the largest Fermi surface area. The two maxima in the density of states are found near one and eight *d*-electrons per atom. Conversely, the minimum Fermi surface is found near five *d*-electrons per atom, the electron concentration where there is no Jahn−Teller driving force.

These coincidences can again be accounted for by examining the ΔE_{star} function. We consider here 7.8 e^-/a, the band-filling where the driving force to the distorted bct structure is strongest. At this electron count, ΔE_{star} has a maximum near $\vec{k} = (0, {}^1/_2, {}^1/_2)$, a *k*-point traditionally termed *M*.[86] In Figure 13a, we give ΔE_{star} for the plane $\vec{k} = (0, k_y, k_z)$. It can be seen that ΔE_{star} is nearly zero except around *M*. This peak extends quite far in the k_x direction. Even in the $\vec{k} = (0.2, k_y, k_z)$ plane, see Figure 13b, it is still quite prominent.

As in the previous two-dimensional example, we can trace the origin of this peak to the corresponding crystal orbitals. In Figure 14a we show a portion of the band diagram for a bcc cell between *M* and *R* $\{\vec{k} = ({}^1/_2, {}^1/_2, {}^1/_2)\}$. We choose this segment of *k*-space as it is along this direction that ΔE_{star} is large. All the bands between *M* and *R* are doubly degenerate. Two of these bands track closely to one another, never differing in energy by more than a few hundreths of an electronvolt. At *M* they have an energy of −10.64 eV, the Fermi energy of the 7.8 e^-/a system. In Figure 14b we consider this same region of *k*-space, but with a bct cell with a *c*/*a* axis ratio of 1.026. Under this bct distortion, the bands remain doubly degenerate, but the two bands no longer track each other quite as closely. While at M_z $\{\vec{k} = ({}^1/_2, {}^1/_2, 0)\}$ they are still within 0.06 eV of one another, at M_x $\{\vec{k} = (0, {}^1/_2, {}^1/_2)\}$ they are separated by almost 0.3 eV, a large change considering that the nearest neighbor bond distances have shifted by only 0.004 Å and second nearest neighbor bond distances by 0.05 Å.

The origin of this large energy splitting can be understood if we examine the actual orbitals at M_x. These are shown to the right in Figure 14b. Here we show per band just one of the pair of degenerate orbitals. The lower energy orbital has nearly perfect d_{z^2} atomic orbitals at the unit cell corners, and a smaller d_{xz} atomic orbital at the body center. The higher energy orbital is related by a 90° rotation to the lower energy orbital.

In a bcc cell, the nearest neighbor interactions are between the atoms at the cell corner and the atoms at the body center. Second nearest neighbor interactions are between atoms at adjacent corners. Consider the first nearest neighbor effects. The key point here is that while the body center d_{xz} orbitals are pointing in a σ fashion to the cell corners, the corner atoms are of d_{z^2} and d_{y^2} type. These latter orbitals have a σ-nodal cone at azimuthal angles of 54°. But that is precisely the angle at which the body center atom sits. Hence in bcc there is no σ-interaction between first nearest neighbors. If we now consider $c/a > 1.0$, the body center atom no longer sits on the nodal cone. The lower and higher energy crystal orbitals become respectively σ-bonding and antibonding.

With respect to the second nearest neighbor interactions, the lower energy orbital is seen as principally antibonding along the *z* direction and then weakly bonding in the *xy*-plane. By contrast the higher energy crystal orbital is net antibonding in the *xy*-plane. The bct distortion being considered is one where $c/a > 1.0$. Hence the cell is stretched along the *z* direction and contracted in the *xy*-plane. Therefore, second nearest neighbor effects also cause a substantial Jahn−Teller splitting. In summary both first and second nearest neighbor effects conspire to produce a maximal Jahn−Teller splitting at 7.8 e^-/a at the *k*-point *M*.

Fcc to Fct Distortion. The above results give a clear picture of the Jahn−Teller instabilities of the bcc structure. They suggest only group 5 and 6 elements should be found in the bcc structure. This is confirmed experimentally: the only bcc transition elements are V, Nb, Ta, Cr, Mo, and W. But the above analysis is not complete. All we have shown so far is that group 7 and higher or group 4 and lower elements are Jahn−Teller unstable in the bcc structure. It is possible that closest packed structures are Jahn−Teller unstable as well. We therefore turn to distortions of a fcc cell. We consider face centered tetragonal (fct) distortions to this fcc cell. This is illustrated in Figure 15.

In Figure 16a we compare the differences in energy between an fcc cell and an fct cell ($c/a = 0.98$), using both the μ_2-Hückel method and an integrated ΔE_{star} function. As in the previous cases, the two functions closely track one another. It is also instructive to compare Figure 16a with Figure 12a. It may be seen that the two figures are complements of each other. At 4 or 5 *d*-electrons per atom the fcc structure is unstable with respect to a flattened tetragonal cell but at the same electron count bcc is stable. By contrast at 6 to 9 *d*-electrons per atom bcc is unstable with respect to an elongated tetragonal cell but fcc is stable. A sufficiently flattened fct cell is bcc, just as a sufficiently elongated bct cell is fcc. Hence these results are compatible with 4 or 5 *d*-electron per atom cells flattening until

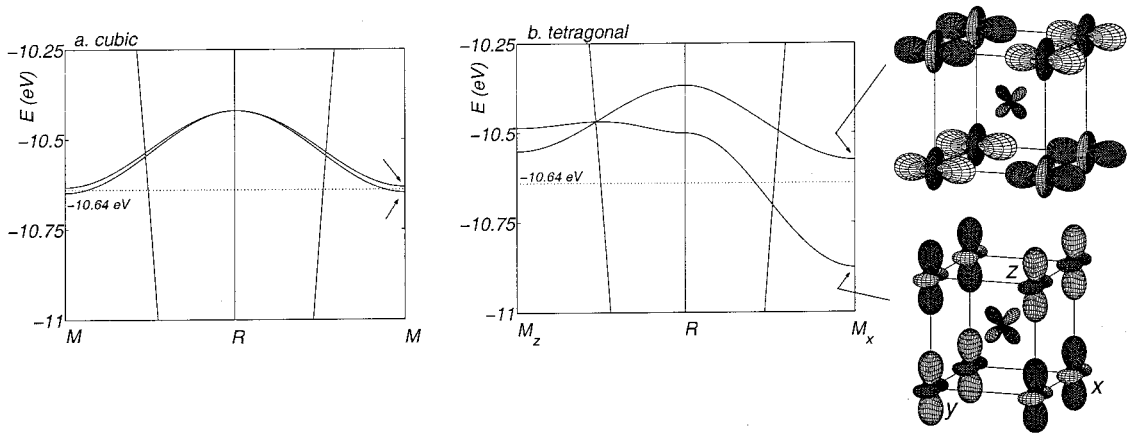

Figure 14. Band diagram for the *d*-orbital only model between M and R,(a) for bcc and (b) for bct ($c/a = 1.026$). The Fermi energy of the 7.8 e^-/a bcc system is −10.64 eV. The key orbitals for ΔE_{star} are indicated by arrows. For the sake of clarity body center atomic orbitals have been increased by 20%.

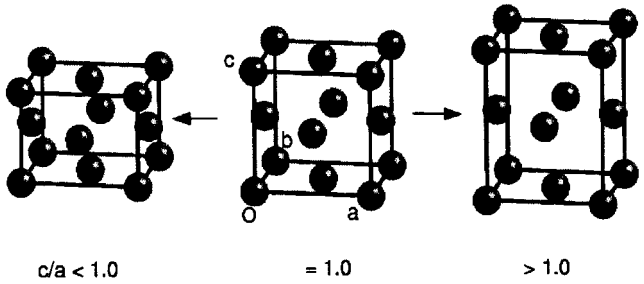

Figure 15. D_{4h} to O_h to D_{4h} distortion for a face centered tetragonal lattice.

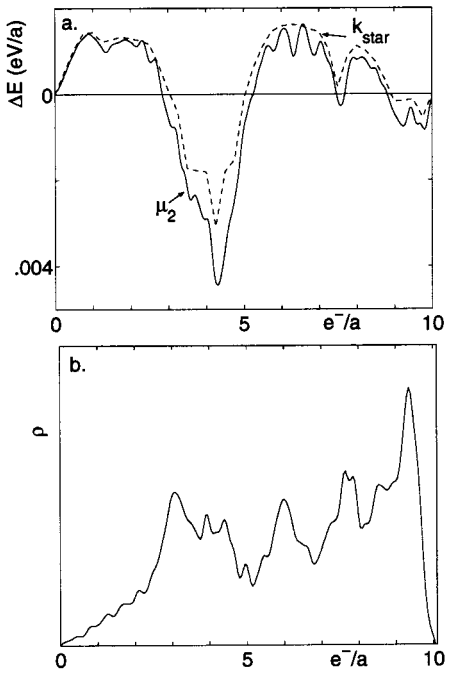

Figure 16. (a) Difference in energies between fcc and fct ($c/a = 0.98$) using a *d*-orbital only model. Negative values correspond to fct being more stable. (b) Electronic density of states for fcc given as a function of *d*-orbital band-filling.

they become bcc and 6−9 *d*-electron per atom bct cells elongating until they are ideally fcc. Recalling that at the half-filled band there is approximately one electron in an *s*-orbital per atom, these results suggest that at 6 e^-/a, bcc should be an energy minimum structure and fcc a saddlepoint, while at 7 e^-/a, the roles of bcc and fcc should be reversed. As W has 6 e^-/a and Re and TaIr an average of 7 e^-/a, these qualitative theoretical calculations match precisely the DFT results illustrated in Figure 2.

In Figure 16b we show the electronic density of states as a function of band filling. In contrast to the preceding cases, we see there is little agreement between the maxima and minima of parts a and b of Figure 16. Recalling our analysis of the source of these coincidences, we therefore anticipate that the key *k*-vectors for ΔE_{star} do not lie at the corners in *k*-space. That this is so is verified by explicitly calculating ΔE_{star} at 4.2 *d*-electrons per atom, the electron concentration with the greatest driving force for the fct distortion.

The principal features in the fcc to fct ΔE_{star} landscape are a plateau found near $\vec{k} = (1/4, 1/4, 1/4)$ and a circular ring of states between $\vec{k} = (1/4, 1/4, 1/4)$, (0.37, 0.37, 0.37), and (0.5, 0.3, 0.3). These are illustrated in Figure 17. We may account for these features by examining the corresponding crystal orbitals. In Figure 18a we present a band diagram between Γ and *R*. It can be seen that along this segment of *k*-space there are two sets of degenerate bands at the Fermi energy of −12.9 eV. There is a doubly degenerate band near $\vec{k} = (1/4, 1/4, 1/4)$, and a triply degenerate band near (0.37, 0.37, 0.37). Under a small fct distortion to $c/a = 0.97$, these bands split by respectively 0.4 and 0.3 eV (see Figure 18b).

Again we turn to the shapes of the crystal orbitals to account for this splitting. As these orbitals do not lie at special points in *k*-space, the corresponding crystal orbitals have complex coefficients. To give understandable graphical representations, we substitute the orbitals at *R* most closely correlated to the true orbitals at (0.37, 0.37, 0.37). These are shown to the right of Figure 18b. As may be seen in this figure, the lower energy orbital is σ-bonding along the $y + z$ direction across the *yz* face of the cube, σ-bonding along the $x + z$ direction across the *xz* face of the cube, but π-antibonding along the $x - y$ direction across the *xy* face. Similarly, the higher energy orbital is antibonding along the *z* direction but σ-bonding along the $x + y$ direction across the *xy* face. A flattening of the unit cell splits these two orbitals apart, the classic Jahn−Teller scenario. A similar diagram can be made at (0.5, 0.3, 0.3).

The orbitals at $\vec{k} = (1/4, 1/4, 1/4)$ are also complex, but here atomic coefficients can be made purely real or purely imaginary. As there is no interaction between a real and an imaginary orbital, and as in this case the real and imaginary coefficients

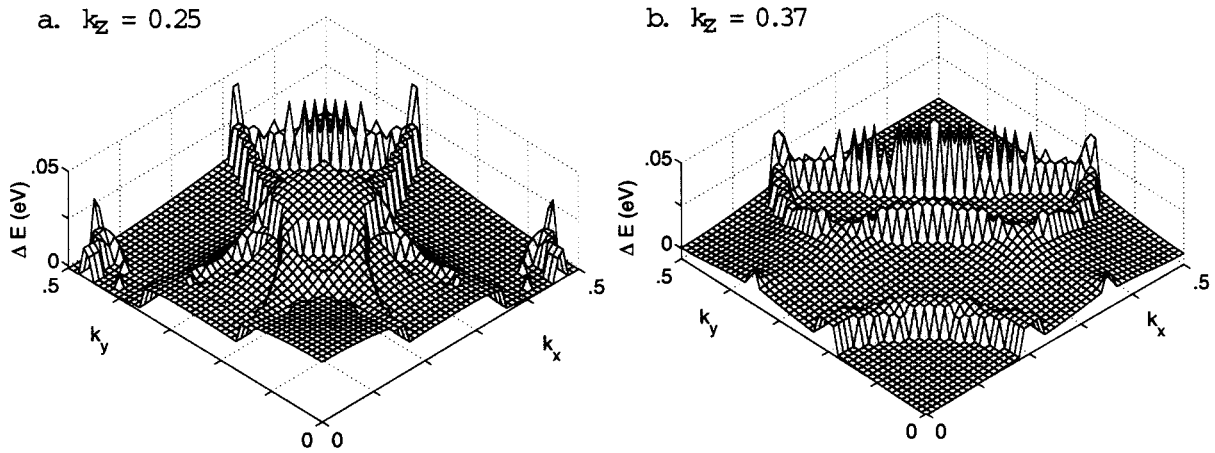

Figure 17. ΔE_{star} for 4.2 e^-/a for fcc and fct ($c/a = 0.98$) using a *d*-orbital only model for (a) the $\vec{k} = (k_x, k_y, 0.25)$ plane and (b) the $\vec{k} = (k_x, k_y, 0.37)$ plane.

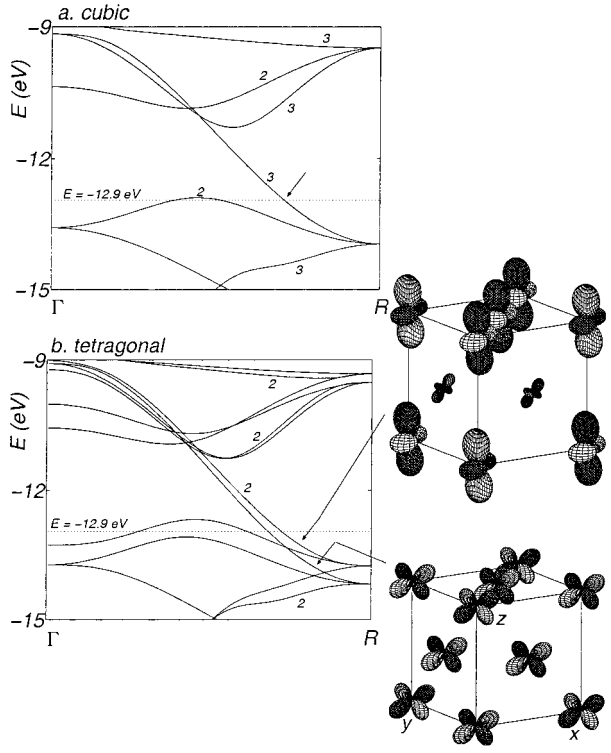

Figure 18. Band diagram for the *d*-orbital only model between Γ and R (a) for fcc and (b) for fct ($c/a = 0.97$). Numbers indicate the band degeneracies. The Fermi energy of the 4.2 e^-/a bcc system is −12.90 eV. Some of the key orbitals of ΔE_{star} are indicated by arrows.

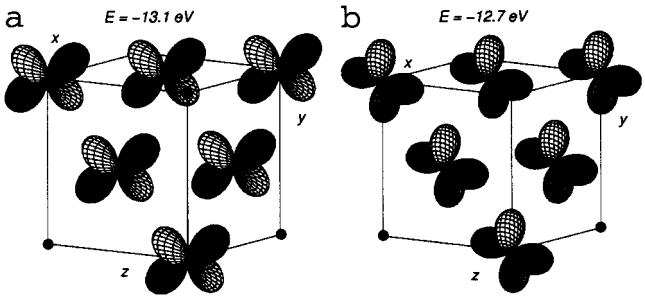

Figure 19. Real portion of fct ($c/a = 0.97$) orbitals at $\vec{k} = (1/4, 1/4, 1/4)$.

on neighboring atoms are similar, to get a sense of its bonding nature, we can portray just the real portion of the orbital. These real portions are shown in Figure 19. The lower energy orbital is π-antibonding in the *xy* plane but σ-bonding in the *z* direction. Its energy is therefore lowered by the fct distortion. The higher energy orbital is σ-bonding in the *y* direction but π-antibonding in the $y + z$ direction. Its energy is raised by the fct distorion, causing a large Jahn−Teller splitting.

Bcc, Fcc, and Bct Binary Alloys. It is well established that electron counting rules true for the elements often also apply to their alloy and intermetallic counterparts.[95,96] Here we consider the relevance of the above theoretical treatment to fully atomically ordered,[97] magnetically unordered,[98] low-temperature stable[92] binary transition metal alloys of group 4 through 9 elements. We are interested in atomically ordered phases, as these are the ones most easily amenable to band structure calculations. We restrict ourselves to magnetically unordered, low-temperature stable phases, as we have not considered spin interactions or entropy effects. Finally we consider only group 4−9 binary alloys, since it is only for transition metals of fairly similar orbital character that the μ_2-Hückel method can be applied. In Table 1, we list all phases which form in variants of the bcc, fcc, and bct structures and where the stoichiometries of the two elements are either 1:1 or 1:3.[97,99] The 1:2 ratio transition metal alloys tend to form in Laves phases and hence are not often structurally related to bcc, bct, or fcc.

Three main structure types are found. The first is the well-known CsCl structure, a cubic structure with one atom at the corner of the unit cell and the other atom type at the body center. It is an ordered bcc cell. The second is $AuCu_3$, a structure with an fcc network of atoms, with one atom type on the cubic unit cell corner and the other on the cell faces. Finally, and most interestingly, there is the HgMn structure, also called the AuCu I structure. Unlike the previous two structures, this type is tetragonal. This is an ordered bct arrangement with one atom at the cell corner, and the other atom at the body center.

All three structures are therefore ordered variants of bct, see Figures 1a and 3. In Table 1 we list for each of the compounds

(95) Hume-Rothery, W.; Raynor, G. V. *The Structure of Metals and Alloys*; Institute of Metals, London: 1962.
(96) Hume-Rothery, W. *Phase Stability in Metals and Alloys*; McGraw-Hill, New York: 1965.
(97) Villars, P.; Calvert, L. D. *Pearson's Handbook of Crystallographic Data for Intermettallic Phases*; ASM International: Materials Park, OH, 1991.
(98) Wijn, H. P. J., Ed. *Landoldt-Börnstein New Series*: *Group 3*: *Condensed Matter*, *Volume 19*: *Magnetic Properties of Metals*, *Subvolume a*: *3d, 4d, 5d-Elements, Alloys, and Compounds*; Springer: Berlin, Germany, 1986.
(99) van Vucht, J. H. N. *J. Less Comm. Met.* **1966**, *11*, 308.

Table 1. Atomically Ordered, Magnetically Unordered, Low Temperature Binary Bcc, Bct and Fcc Compounds

compd	structure type	e^-/a	c/a
TiTc	CsCl	5.50	1.00
HfTc	CsCl	5.50	1.00
VMn	CsCl	6.00	1.00
VTc	CsCl	6.00	1.00
HfRu	CsCl	6.00	1.00
TiOs	CsCl	6.00	1.00
ZrOs	CsCl	6.00	1.00
HfOs	CsCl	6.00	1.00
ZrCo	CsCl	6.50	1.00
HfRh	CsCl	6.50	1.00
TaRu	HgMn	6.50	1.02
NbRu	HgMn	6.50	1.12
TiRh	HgMn	6.50	1.14
TiIr	HgMn	6.50	1.18
MnIr	HgMn	8.00	1.34
$NbRu_3$	$AuCu_3$	7.25	1.41
$TiRh_3$	$AuCu_3$	7.75	1.41
$ZrRh_3$	$AuCu_3$	7.75	1.41
$HfRh_3$	$AuCu_3$	7.75	1.41
$TiIr_3$	$AuCu_3$	7.75	1.41
$ZrIr_3$	$AuCu_3$	7.75	1.41
$HfIr_3$	$AuCu_3$	7.75	1.41
VRh_3	$AuCu_3$	8.00	1.41
$TaRh_3$	$AuCu_3$	8.00	1.41
VIr_3	$AuCu_3$	8.00	1.41
$NbIr_3$	$AuCu_3$	8.00	1.41
$TaIr_3$	$AuCu_3$	8.00	1.41

the c/a ratio in terms of this bct cell and the average number of e^-/a. There is a strong correlation between the two. At 5.5 and 6 e^-/a, the c/a ratio is invariably 1, at 6.5 e^-/a the c/a ratio rises from 1.00 to 1.18, and finally above 7.25 e^-/a, $c/a = \sqrt{2}$. This trend is in agreement with the results of Figure 12a and 16a. As these figures show, at electron concentrations of 5.5 *d*-electrons per atom (or equivalently 6.5 valence electrons per atom), both the fcc vs fct integrated ΔE_{star} function and the bcc vs bct integrated ΔE_{star} function go through a node. Hence bcc, fcc, and bct structures with $1.0 < c/a < \sqrt{2}$ are all comparable in energy. It is exactly here that we find the tetragonal HgMn structures. The one HgMn structure that does not obey this electron count rule is MnIr, a phase whose magnetic structure has not been studied.[98]

These results also suggest why the tetragonal structures are so much rarer than the cubic ones. For such tetragonal structures to occur one needs electron counts where both bcc and fcc are Jahn−Teller unstable. Instead, as Figures 12a and 16a demonstrate, these curves are complements of each other. Only near the nodes of the curves in these figures are distorted bct or fct cells a reasonable energetic alternative.

Conclusion

In studying the interplay of symmetry and crystal energies, solid state chemists and physicists have traditionally focused on translational symmetry elements. In retrospect it is clear why. The preeminent example of a Jahn−Teller distortion in a crystal is the Peierls distortion,[82] a distortion for one-dimensional systems. In one dimension the only point group operation is the inversion center, a symmetry element that due to Friedel's law[100] cannot play a strong energetic role in ΔE_{star}.

In higher dimensional crystal distortions, there is generally loss of both translational and rotational symmetry elements. Given the importance of the Peierls distortion, it is natural that we should focus on the former and not the latter group elements. It is nonetheless plausible that by concentrating solely on the translational elements, vital factors governing structural distortions have been ignored.

Studies involving loss of translational symmetry have demonstrated the power of maximal Fermi surface nesting, i.e., of *k*-vectors which maximally couple Fermi surface states.[85] This can be directly contrasted to the analysis in the current work. We have found that distortion is not just driven by the number of Fermi surface states, but also by the propensity of these states and their corresponding orbitals for distortion. Indeed others have found smilar effects, for example, when studying electron−phonon coupling.[87] In one system we studied, fcc vs fct, these latter propensities were a more important factor than the area of Fermi states. It would be interesting to determine if there are other systems where both translational and rotational symmetry elements play a role and where similar orbital propensities dominate. In such phases the maximal nesting vector might not be observed, instead a seemingly lesser nesting vector could be adopted due to its superior orbital interactions.

Acknowledgment. This work was supported by the National Science Foundation (Grant DMR-0073587) and by the Petroleum Research Fund, administered by the American Chemical Society. We wish to thank Dr. Evgeny Todorov without whose strong interest this project would not have been completed.

JA0114557

(100) Friedel, G. *Comptes Rendus* **1913**, *157*, 1533.